

Basin-scale reconstruction of euxinia and Late Devonian mass extinctions

<https://doi.org/10.1038/s41586-023-05716-2>

Received: 20 January 2022

Accepted: 9 January 2023

Published online: 8 March 2023

 Check for updates

Swapan K. Sahoo^{1,9}✉, Geoffrey J. Gilleaudeau^{2,9}, Kathleen Wilson³, Bruce Hart^{1,4}, Ben D. Barnes⁵, Tytrice Faison⁶, Andrew R. Bowman⁷, Toti E. Larson⁸ & Alan J. Kaufman^{6,9}

The Devonian–Carboniferous transition marks a fundamental shift in the surface environment primarily related to changes in ocean–atmosphere oxidation states^{1,2}, resulting from the continued proliferation of vascular land plants that stimulated the hydrological cycle and continental weathering^{3,4}, glacioeustasy^{5,6}, eutrophication and anoxic expansion in epicontinental seas^{3,4}, and mass extinction events^{2,7,8}. Here we present a comprehensive spatial and temporal compilation of geochemical data from 90 cores across the entire Bakken Shale (Williston Basin, North America). Our dataset allows for the detailed documentation of stepwise transgressions of toxic euxinic waters into the shallow oceans that drove a series of Late Devonian extinction events. Other Phanerozoic extinctions have also been related to the expansion of shallow-water euxinia, indicating that hydrogen sulfide toxicity was a key driver of Phanerozoic biodiversity.

The Devonian/Carboniferous (D/C) transition (about 360 million years ago) marks a fundamental shift in the Earth system primarily related to changes in the oxidation state of surface environments that profoundly altered the trajectory of life on Earth^{1,2}. The pulsed biotic crises of this transition (for example, Annulata⁷, Dasberg⁸ and Hangenberg²) were plausibly linked to complex physical and biogeochemical feedbacks driven in part by the continued evolution and spread of vascular plants in terrestrial environments that enhanced weathering rates, soil formation and the delivery of nutrients to the oceans, while simultaneously transferring carbon from the atmosphere to Earth's surface and water from the surface to the atmosphere through photosynthesis and evapotranspiration, respectively^{3,4}. The continued spread of terrestrial plants may thus have resulted in long-term climatic cooling⁵, the expansion of continental ice sheets⁶ and a shift in the redox balance of the ocean–land–atmosphere system, including widespread deposition of anoxic black shale in epicontinental seas^{3,4}. In this study, we present an integrated sedimentological and geochemical study of black shale from the Bakken Formation (Williston Basin, USA) that spans three key Late Devonian biotic events. High-stratigraphic-resolution mineralogical, elemental and biogeochemical data from two continuous drill cores, and redox-sensitive elemental data from an additional 90 drill cores, provide a spatiotemporal window into sea-level, climate, redox and extinction events across the D/C transition.

During the mid- to late Palaeozoic transition, the North American craton was flooded by a series of epicontinental seas with variable connectivity to the open ocean⁹ (Fig. 1). The sediments that accumulated in the Williston Basin comprise Famennian evaporites of the Three Forks Formation and petrolierous Lower Bakken Shale (LBS); carbonaceous sandstone of the Middle Bakken (MB) Formation that accumulated during glacioeustatic fall and subsequent post-glacial rise across the D/C boundary⁶; the Tournaisian Upper Bakken Shale (UBS) deposited during

continued transgression; and the Lodgepole Limestone, representing carbonate platform development (Fig. 1)^{10,11}. The LBS is divided into four subunits (LB1, LB2, LB3 and LB4) with boundaries marked by regionally traceable carbonate concretion layers (Supplementary Fig. 5). Relative sea-level change has been inferred from gamma logs, calcium contents and fluctuations in detrital indicators. On the basis of these criteria, black shale of LB1, LB2 and LB3 represent discrete pulses of marine transgression, with maximum flooding in LB3 followed by marine regression in LB4 that transitions to lowstand deposits of the first member of the MB (MB1). Post-glacial transgression initially occurs in the second member of the MB (MB2), and the overlying UBS is subdivided into UB1 and UB2, representing a broad, continued transgression^{10,11}.

In this study, we used the Sjol (Extended Data Fig. 1) and Charlie Sorenson cores to create a composite that represents the entire succession (Fig. 2). Previous conodont biostratigraphy has suggested that LB1, LB2 and LB3 were coincident with three globally recognized Late Devonian biotic crises—the Annulata, Dasberg and Hangenberg black shale events, respectively¹¹. In the Sjol core, the conodont *Bispathodus aculeatus aculeatus* through *Bispathodus ultimus* zones were identified from the middle of LB2 to LB3, suggesting correlation of LB3 with the Hangenberg black shale in Europe according to the conodont zonation scheme of refs. ^{12,13} (Extended Data Fig. 2). Furthermore, the Hangenberg black shale—which marks the beginning of the main extinction episode of the Hangenberg biotic crisis¹⁴—is associated with eustatic rise and the development of anoxic facies across multiple continents^{2,14,15}, corresponding to maximum transgression in LB3 of the Williston Basin. No biostratigraphy is available for the Charlie Sorenson core, but ref. ¹¹ studied conodonts in the nearby (about 12 km) Person core, identifying the *Palmatolepis gracilis expansa* Zone in LB2, thereby supporting its equivalence with the Dasberg Event. The same authors identified the conodont *Pseudopolygnathus granulosus*, *Polygnathus styriacus*

¹Equinor US, Houston, TX, USA. ²George Mason University, Fairfax, VA, USA. ³Boston College, Chestnut Hill, MA, USA. ⁴University of Western Ontario, London, Ontario, Canada. ⁵Pennsylvania State University, University Park, PA, USA. ⁶University of Maryland, College Park, MD, USA. ⁷Gaia Paleontological Services LLC, Missouri City, TX, USA. ⁸Bureau of Economic Geology, University of Texas at Austin, Austin, TX, USA. ⁹These authors contributed equally: Swapna K. Sahoo, Geoffrey J. Gilleaudeau, Alan J. Kaufman. ✉e-mail: swas@equinor.com

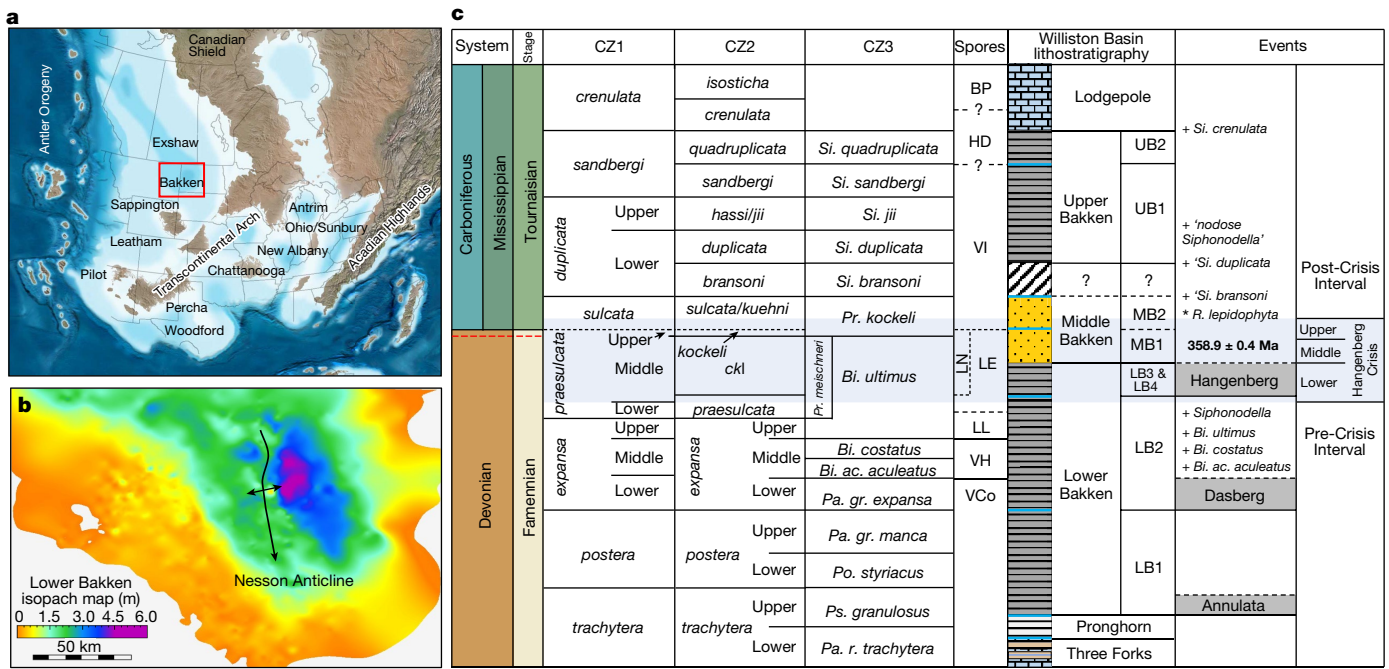


Fig. 1 | Geological setting of the Famennian–Tournaisian successions of the Williston Basin, USA and Canada. a, Late Devonian North American palaeogeography and location of North American formations⁹. The map was obtained from “Key Time Slices of North America © 2013 Colorado Plateau Geosystems Inc.”⁹. The Williston Basin was located at equatorial southern latitudes in the Late Devonian. **b,** Isopach map of the Williston Basin during Lower Bakken deposition. This also represents relative estimated water depths in the basin during the Late Devonian. **c,** Biostratigraphic and lithostratigraphic correlation of sections is based on conodont and miospore biozones^{11–14,45–50}. Different conodont schemes are represented by CZ1, CZ2 and CZ3, where CZ1 is “standard” zonation^{46,47}, CZ2 is based on the presence of the extinction-based *costatus*–*kockeli* Interregnum (*ckl*)^{2,14,48} and CZ3 is based on the *Bispathodus ultimus* and *Protognathodus meischneri* zones^{12,13}. Spore zones are from ref.⁴⁹. The D/C boundary is currently defined by the first occurrence of *Siphonodella*

sulcata, which is the base of the *sulcata*/*kuehni* Zone (CZ2), or the base of the *sulcata* Zone (CZ1), respectively (black dashed line). In CZ3, the base of the enlarged *Pr. kockeli* Zone marks the D/C boundary (red dashed line)^{45,50}. The blue shaded bar denotes the Hangenberg Crisis interval². The light blue lines on the lithostratigraphic column represent flooding surfaces. For global correlations, the events column shows the major events in Rhenish successions, Germany^{2,14}. LB, Lower Bakken; UB, Upper Bakken; MB, Middle Bakken. For conodont taxa: *Pa.*, *Palmatolepis*; *r.*, *rugosa*; *Ps.*, *Pseudopolygnathus*; *Po.*, *Polygnathus*; *gr.*, *gracilis*; *Bi.*, *Bispathodus*; *ac.*, *aculeatus*; *Pr.*, *Protognathodus*; *Si.*, *Siphonodella*. The first appearance datum is represented by a plus sign, and extinction is represented by an asterisk in the events column. Grey zoned boxes represent the three biotic crises examined in this study: the Annulata, Dasberg and Hangenberg extinction events. The age of the D/C boundary is defined as 358.9 ± 0.4 million years ago by the International Commission on Stratigraphy.

and *Palmatolepis gracilis manca* zones in LB1, suggesting correlation with the Annulata Event (see refs.^{2,7,16,17} for palaeontological review).

Using a suite of wet chemical laboratory extractions and mass spectrometric techniques (Methods) on samples from these two cores, we determined the relative distribution of iron (Fe) between carbonate, oxide, silicate and sulfide minerals, and the concentration of trace metals molybdenum (Mo), vanadium (V), uranium (U), zinc (Zn) and rhenium (Re), as redox proxies. Iron speciation results indicate persistently euxinic (anoxic + sulfidic) conditions during deposition of the LBS¹⁷. Molybdenum concentrations increase up-section in three distinct pulses corresponding to LB1, LB2 and LB3. We suggest that the pulsed Mo enrichment (with maximum concentrations of about 600 ppm in LB3) resulted from progressive flushing of the basin with Mo from the global ocean reservoir, as well as intensification of water-column euxinia (and metal sequestration in sediments) during each transgressive event^{18–21}. Vanadium abundances remain near crustal values (upper continental crust [V] = 97 ppm)²² in LB1, show minor enrichment during the second transgressive pulse in LB2 and then become highly enriched in LB3 (>2,000 ppm). These data suggest that the V inventory of the basin remained low during deposition of LB1, increased in LB2, and then further flushing of the basin with V during maximal transgression and intensification of water-column euxinia led to strong V enrichments in LB3. In the LBS, Re increases alongside Mo—which supports the interpretation of a sulfidic water column²¹—and Zn behaves similarly to V, with Zn showing hyper-enrichments in LB3 (up to about 2,000 ppm) that ref.²³ attributed to the activity of phototrophic sulfide-oxidizing

bacteria, thus indicating photic zone euxinia (PZE). This is consistent with biomarker evidence for PZE in LB3 from a Canadian core²⁴. Together, iron speciation and trace-metal data indicate that Late Devonian marine transgressions flushed metals into the basin that were sequestered in sediments due to the intensification of water-column euxinia, with maximum flooding and extent of euxinia achieved in LB3.

Biogeochemical data are consistent with interpretations drawn from the sea-level history and redox geochemistry of the LBS. Total organic carbon (TOC) and total nitrogen (TN) progressively increase through LB1, increase again at the base of LB2, and peak with values near 20 wt% and 0.6 wt%, respectively, in LB3, indicating strongly reducing bottom-water conditions. Analogous to the trace-metal patterns, the nitrogen isotope ($\delta^{15}\text{N}$) profile reveals three distinct positive excursions associated with LB1, LB2 and LB3. This pattern culminates with the highest $\delta^{15}\text{N}$ values associated with maximum metal enrichments in LB3. In the modern ocean, ammonia produced from microbial nitrogen fixation (typically oxidized to nitrate) has an isotopic composition near 0‰. Denitrification subsequently transfers isotopically light ^{14}N back to the atmosphere, leaving the residual oceanic nitrate pool enriched in ^{15}N (ref.²⁵). Denitrification occurs in modern oxygen minimum zones and intensifies in the water column under anoxic conditions; thus, a shift towards higher $\delta^{15}\text{N}$ values in the ancient record is often interpreted as a local intensification of anoxia^{26,27}. Alternatively, in highly restricted basins, pervasively anoxic conditions could hinder the oxidation of ammonia to nitrate, and hence preclude microbial denitrification. Under these conditions, available N in the restricted water column

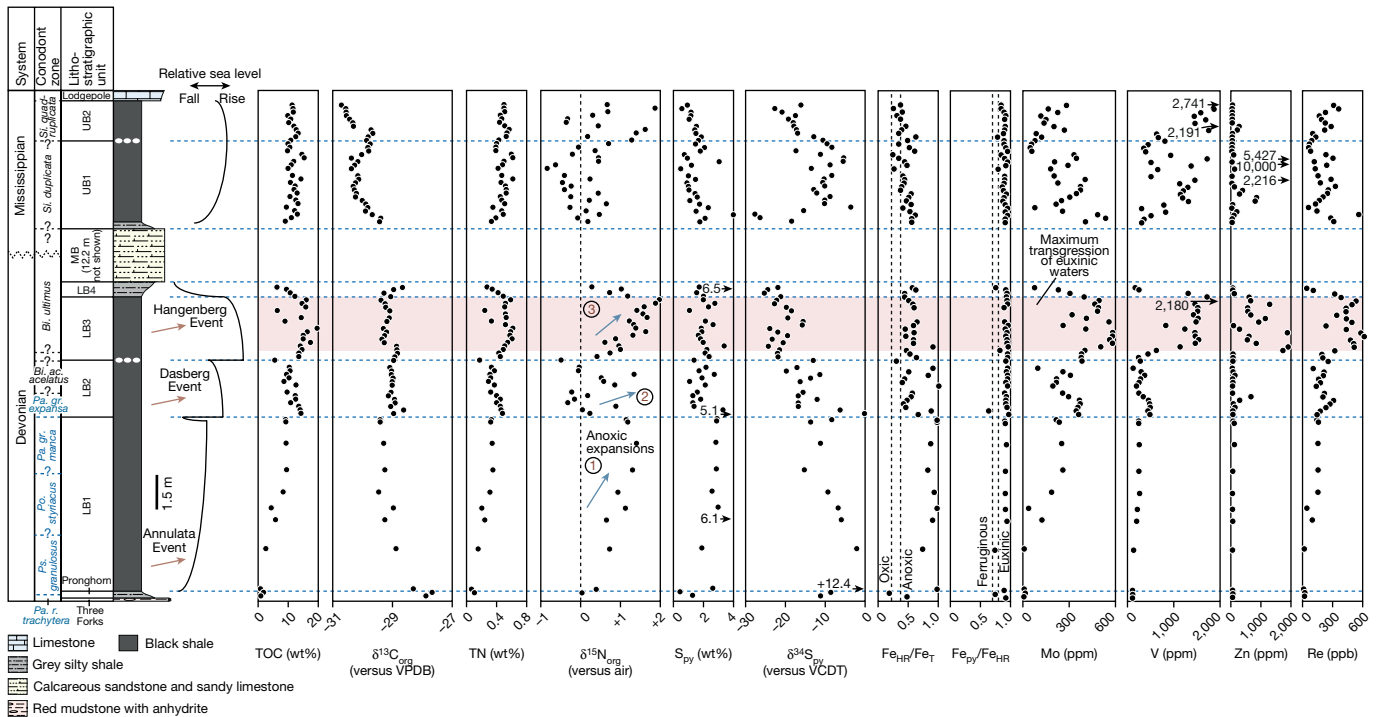


Fig. 2 | Lithostratigraphy, biostratigraphy, sea-level history and time-series geochemistry of the composite section constructed from the Sjol and Charlie Sorenson cores, North Dakota, USA. White ovals on the stratigraphic column represent carbonate concretion horizons. For visual purposes, 12.2 m of the Middle Bakken Formation are not shown. Cut-off values for iron speciation interpretations are represented by vertical dashed lines in the iron speciation columns. The horizontal blue dashed lines delineate subunit boundaries identified using carbonate concretion layers. Conodont biostratigraphy was performed on the Sjol core with identified zones in LB2 and LB3 shown in black using the CZ3 conodont zonation scheme. In addition, the *crenulata* Zone (CZ1 and CZ2) was identified in the Lodgepole Limestone in the Sjol core. Conodont biostratigraphy from LB1 comes from ref.¹¹, which investigated the Person core drilled about 12 km from the Charlie Sorenson

core. Conodont zones from ref.¹¹ are shown in blue and follow the CZ3 classification in Fig. 1. These conodont data provide our best estimate of the position of the Annulata, Dasberg and Hangenberg events in our composite section. High-resolution placement of these events at exact stratigraphic horizons is not possible in the Bakken Shale because these events are not characterized by distinct facies changes (in contrast to European sections³³) and due to insufficient resolution in conodont biostratigraphic data. $\delta^{13}\text{C}_{\text{org}}$ and $\delta^{15}\text{N}_{\text{org}}$ refer to the isotopic composition of organic carbon and nitrogen, respectively. Fe_{HR} , highly reactive iron; Fe_{py} , pyrite iron; and Fe_t , total iron. In the $\delta^{15}\text{N}$ profile, the blue arrows highlight the positive excursions and the circled numbers represent the three proposed anoxic expansions. The pink shaded bar represents the interval of maximum euxinic expansion during the Hangenberg Event.

would retain atmospheric $\delta^{15}\text{N}$ values near 0‰. In contrast, the presence of nitrate in the more oxidized open ocean would have resulted in higher $\delta^{15}\text{N}$ values; thus, a shift towards higher $\delta^{15}\text{N}$ values in the Williston Basin could also indicate the influx of ^{15}N -enriched waters from the open ocean during marine transgression. Within this framework, the three $\delta^{15}\text{N}$ increases in LB1, LB2 and LB3 can be interpreted as: (1) three intervals of local intensification of anoxia, (2) three transgressive injections of ^{15}N -enriched waters into the Williston Basin, or (3) a combination of these processes. The positive $\delta^{15}\text{N}$ excursion in LB3 is similar in magnitude to a $\delta^{15}\text{N}$ excursion in the Famennian Cleveland Shale (Appalachian Basin), with both horizons potentially deposited across the Hangenberg Event (Supplementary Fig. 22)^{28,29}. Lastly, pyrite sulfur isotope ($\delta^{34}\text{S}_{\text{py}}$) values markedly decrease from 0 to nearly -30‰ through the LBS, with minimum values recorded in LB3 coincident with the highest $\delta^{15}\text{N}$ values and the strongest trace-metal enrichments. We interpret this pattern in two ways: (1) progressive flushing of the basin with marine sulfate upon marine transgression thereby increasing the magnitude of microbial fractionation between sulfate and sulfide; and (2) progressive intensification of water-column euxinia, which drove the formation of syngenetic pyrite in the water column¹⁹. Syngenetic pyrite formation is supported by a positive intercept on the sulfur (S) axis in a scatter plot of TOC versus total S in the Bakken Shale³⁰. Both interpretations are consistent with our integrated model of stepwise marine transgression and intensification of water-column euxinia as major drivers of the Annulata, Dasberg and Hangenberg biotic crises.

Spatiotemporal redox trends across the entire Williston Basin were mapped using X-ray fluorescence (XRF) trace-metal data from 90 cores representing about 11,000 data points (for locations, see Extended Data Fig. 3). Basin-scale gridded heat maps (Fig. 3) show spatial variations in Mo and V concentrations in each of LB1, LB2 and LB3. Gridded cross-sections (Fig. 4) drawn with the Ocean Data View tool show variations in Mo and V concentrations across an east–west-oriented dip-line. The heat maps reveal the spatial extent of LB1, LB2 and LB3 deposition (Fig. 3), with LB1 restricted to the central, deepest portion of the basin (an area of about 6,000 km²) associated with limited marine flooding. LB2 is spatially expanded (about 27,000 km²) as marine flooding progressed, and LB3 covers the maximum spatial extent (about 160,000 km² in the United States) associated with maximum transgression. Trace-metal enrichments follow this sea-level history, with strong Mo and V enrichments in sediments indicative of water-column euxinia^{18–20}. In LB1, Mo abundances across the basin are moderate (median 212 ppm, $n = 885$) with a locus of Mo enrichment in the southeast, which could be due to a shallower basin geometry. Vanadium is not strongly enriched above crustal values across much of the basin in LB1 (median 218 ppm, $n = 885$), with only a slight increase also seen in the southeast. As transgression continued and the spatial extent of sedimentation widened in LB2, Mo and V concentrations show corresponding increases (median 299 ppm and 399 ppm, respectively, $n = 2,548$). Notably, the locus of Mo and V enrichment (and thus water-column euxinia) occurs concentrically around the edges of the flooded basin in the

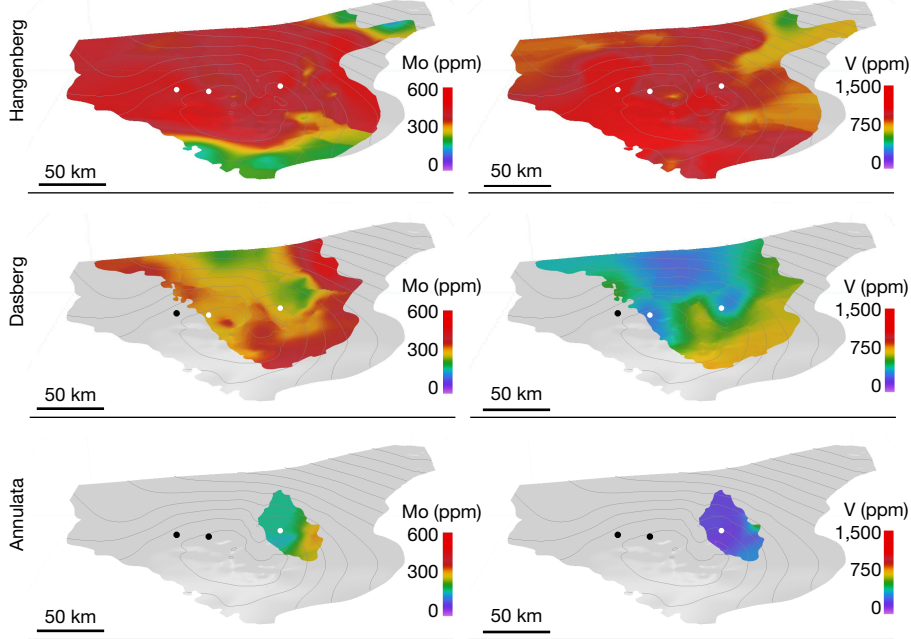


Fig. 3 | Basin-scale metal distribution heat maps. Individual maps show spatial variations in Mo and V concentrations in each of LB1 (Annulata), LB2 (Dasberg) and LB3 (Hangenberg) subunits and events across the Williston Basin in the United States. The base map is a palaeo-depth structure map of the LBS with 1–2° slope. The edge of the map is derived from the maximum areal extent of the LBS in regional multi-well studies^{10,30}. The top boundary is the United States–Canada border. The Mo and V concentration map grids were derived from the POFG dataset (75 wells), in addition to previous literature data

compilation (15 wells) (see Extended Data Fig. 3 and Supplementary Table 1c for locations and references). A total of about 11,000 data points were used to grid the heat maps. A kriging method was applied for map grids, where an average value was taken from each location for each subunit. It is noted that there is a stepwise increase of sea level through LB1, LB2 and LB3, corresponding to the three extinction events. For reference, three well locations (from west to east: Abe, Sjol and Charlie Sorenson) have been added to represent the flooding of the basin during LB1, LB2 and LB3.

shallowest-water, nearshore environments. The greatest Mo enrichment occurs on the eastern edge of the basin in shallow water. This indicates that progressive marine flooding was associated not only with expanded water-column euxinia, but also specifically with onlapping of euxinic, metal-scavenging seawaters into shallow environments. Maximum transgression is achieved in LB3, associated with maximum Mo and V enrichments (median 416 ppm and 948 ppm, respectively, $n = 3,327$), with the locus of metal enrichment (and euxinia) again occurring in the shallowest settings. Hyper-enrichments of V are seen on the western edge of the basin, which is potentially due to proximity to the Antler volcanic arc insofar as these igneous rocks are generally enriched in V relative to the crustal average³¹. Hyper-enrichment of V is also indicative of hyper-sulfidic conditions in the nearshore water column²³.

These patterns can also be visualized in our gridded dip-line cross-sections (Fig. 4). Low Mo and V concentrations can be traced across subunit boundaries used to delineate LB1, LB2 and LB3. A clear pattern emerges in this basin-scale spatiotemporal view of progressive marine flooding characterized by stepwise onlapping of euxinic, metal-scavenging seawater. The maximum extent and intensity of euxinia is achieved in LB3 where strong Mo enrichments are seen on both edges of the basin, and V becomes hyper-enriched on the western boundary.

Progressive onlapping of euxinic waters during episodic marine transgression has major implications for Late Devonian mass extinction. Maximum transgression and onlapping of euxinic waters in LB3 is directly analogous to the Hangenberg black shale recognized globally³², and the Annulata and Dasberg events (represented by LB1 and LB2, respectively) are also marked by distinct, transgressive black shale horizons in multiple basins worldwide^{7,8}. Evidence for PZE in the Williston Basin is found during only the Hangenberg Event²⁴—which was the most severe of the three extinctions²—although PZE was also

identified during all three events in several European sections based on biomarker data^{16,17,32,33}. The Annulata and Dasberg events were characterized by regional changes in biotic assemblages, including reduction in conodont diversity and ammonoid faunal overturn^{7,8}. The Hangenberg Event is a seminal biological perturbation in Earth history, representing one of the two largest pulses of Late Devonian mass extinction. The Hangenberg Event markedly affected shallow-water taxa, including metazoan reef communities previously devastated by the Kellwasser Event at the Frasnian/Famennian boundary³⁴, as well as other invertebrates in both the pelagic and benthic realms. Ammonoids, rugose corals, trilobites and ostracods experienced major ecological turnover, stromatoporoids became completely extinct, and foraminifera and acritarchs strongly declined in diversity². Marine vertebrate communities were similarly affected, with major declines in conodonts² and lobe-finned fishes³⁴. The paucity of tetrapod fossils identified in the interval following the Hangenberg Event (Romer's Gap) indicates that terrestrial environments were similarly affected³⁵. This may be related to degassing of hydrogen sulfide from shallow euxinic waters, or the effect of uncontrolled wildfires due to high atmospheric oxygen concentrations³⁶. In the aftermath of the Late Devonian mass extinctions, the ecological structure of Earth's biosphere was fundamentally changed. Crinoids experienced an increase in body size³⁷, cartilaginous and ray-finned fishes diversified rapidly³⁸, and true amphibians, reptiles and synapsids appeared during the subsequent Carboniferous Period³⁹. Similar to our interpretation of shallow-water euxinia causally related to extinction in the Late Devonian, other Phanerozoic extinctions have also been related to expansion of shallow-water euxinia^{40,41}, indicating that hydrogen sulfide toxicity was a fundamental driver of Phanerozoic biodiversity. Overall, this study uses a large spatiotemporal geochemical dataset to provide a four-dimensional visualization of euxinic expansion into the shallow oceans directly associated with mass extinction.

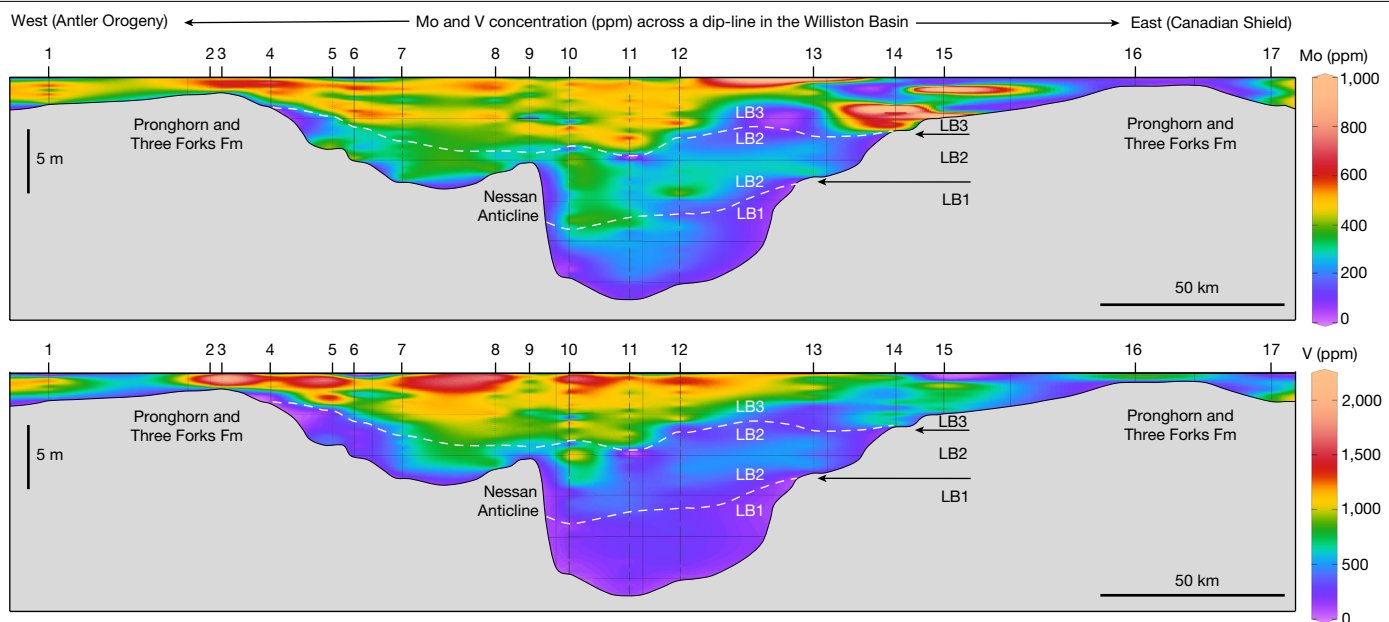


Fig. 4 | Distribution of Mo and V across an east–west-oriented dip-line through the Williston Basin during deposition of the Lower Bakken Shale. Seventeen well sections were selected to best represent the spatial and temporal variation in Mo (top) and V (bottom) concentrations. The base of the Middle Bakken Formation is used as a datum. A total of 2,430 data points was used to grid the cross-section using Ocean Data View (see Methods and Supplementary Information for sample location details; Extended Data Fig. 3

and Supplementary Table 1c). Locations 2, 5 and 11 are the Abe, Sjol and Charlie Sorenson well locations, respectively. The greyed zone represents the presence of the underlying Pronghorn Member and Three Forks Formation (Fm). The white dashed lines delineate the boundaries between subunits LB1, LB2 and LB3. The sharp drop in the bathymetry between location 9 and 10 is due to the Nesson Anticline (see Fig. 1b), which was also present as a regional high during the deposition of the Bakken Formation.

Whereas euxinic expansion in shallow, nearshore areas was an important kill mechanism in Late Devonian extinctions, it need not mean that euxinia was a whole-ocean phenomenon (Methods and Extended Data Fig. 4). Instead, the D/C transition represents a unique interval in Earth history when there was a locus of euxinia and deposition of organic-rich sediments in shallow, epicontinental seas. We suggest that the locus of euxinic expansion in the shallow habitable zone of the oceans contributed to the pattern and severity of Late Devonian mass extinction. Development of widespread epicontinental euxinia was part of a ‘perfect storm’ of conditions that characterized the mid- to late Palaeozoic transition—the continued proliferation of vascular land plants that enhanced both the hydrological cycle and continental weathering; stepwise eustatic rise that flooded craton interiors; enhanced riverine nutrient delivery, eutrophication of epicontinental waters, euxinic expansion and mass extinction; organic carbon burial that (along with enhanced terrestrial photosynthesis) facilitated a long-term transfer of carbon from the atmosphere to geologic reservoirs; and lastly, long-term global cooling, glaciation and the transition to the late Palaeozoic ice age^{3,42}. Extinction and/or development of marine anoxia could also plausibly be linked to volcanism through increased atmospheric partial pressure of carbon dioxide and associated increases in continental weathering intensity and nutrient delivery to the oceans⁴³. Many Hangenberg sections (including the Sjol core) show enrichment in mercury (Hg), which is used as a proxy for volcanic input (Supplementary Figs. 23 and 24)^{32,33,43}. These linked processes (excluding volcanism) are fundamentally different to those recorded during Mesozoic ocean anoxic events where black shales are preserved in deep-water settings (for example, ref. ⁴⁴). The unique palaeoceanographic conditions of the D/C transition also led to worldwide deposition of volumetrically significant hydrocarbon reserves. These transformative events in Earth history are encapsulated in the Bakken Formation, and this study synthesizes a large spatiotemporal dataset that genetically links sea level, climate, ocean chemistry and mass extinction.

Online content

Any methods, additional references, Nature Portfolio reporting summaries, source data, extended data, supplementary information, acknowledgements, peer review information; details of author contributions and competing interests; and statements of data and code availability are available at <https://doi.org/10.1038/s41586-023-05716-2>.

- McGhee, G. R. *The Late Devonian Mass Extinction: The Frasnian/Famennian Crisis* (Columbia Univ. Press, 1996).
- Kaiser, S. I., Aretz, M. & Becker, R. T. The global Hangenberg Crisis (Devonian–Carboniferous transition): review of a first-order mass extinction. *Geol. Soc. Spec. Publ.* **423**, 387–437 (2016).
- Algeo, T. J., Berner, R. A., Maynard, J. B. & Scheckler, S. E. Late Devonian oceanic anoxic events and biotic crisis: ‘rooted’ in the evolution of vascular land plants? *GSA Today* **5**, 63–66 (1995).
- Algeo, T. J. & Scheckler, S. E. Terrestrial–marine teleconnections in the Devonian: links between the evolution of land plants, weathering processes, and marine anoxic events. *Phil. Trans. R. Soc. B* **353**, 113–130 (1998).
- Grossman, E. L. & Joachimski, M. M. In *Geologic Time Scale 2020* (eds Gradstein, F. M. et al.) 279–307 (Elsevier, 2020).
- Isaacson, P. E. et al. Late Devonian–earliest Mississippian glaciation in Gondwanaland and its biogeographic consequences. *Palaeogeogr. Palaeoclimatol. Palaeoecol.* **268**, 126–142 (2008).
- Hartenfels, S. & Becker, R. T. The global Annulata Events: review and new data from the Rheris Basin (northern Taifilt) of SE Morocco. *Geol. Soc. Spec. Publ.* **423**, 291–354 (2016).
- Hartenfels, S. & Becker, R. T. Timing of the global Dasberg Crisis—implications for Famennian eustasy and chronostratigraphy. *Palaeontographica Americana* **63**, 69–95 (2009).
- Blakely, R. *Global Paleogeography and Tectonics in Deep Time Series* (Deep Time Maps Paleogeography, 2016); <https://deeptimemaps.com/global-paleogeography-and-tectonics-in-deep-time/>
- Sonnenberg, S. A., Theloy, C. & Jin, H. The giant continuous oil accumulation in the Bakken petroleum system, U.S. Williston Basin. *AAPG Mem.* **113**, 91–119 (2017).
- Hogancamp, N. J. & Pocknall, D. T. The biostratigraphy of the Bakken Formation: a review and new data. *Stratigraphy* **15**, 197–224 (2018).
- Spalletta, C., Perri, M. C., Jeffrey Over, D. & Corradini, C. Famennian (Upper Devonian) conodont zonation: revised global standard. *Bull. Geosci.* **92**, 31–57 (2017).
- Corradini, C., Spalletta, C., Mosconi, A., Matyja, H. & Over, D. J. Conodonts across the Devonian/Carboniferous boundary: a review and implication for the redefinition of the

- boundary and a proposal for an updated conodont zonation. *Geol. Mag.* **154**, 888–902 (2017).
14. Becker, R. T., Kaiser, S. I. & Aretz, M. Review of chrono-, litho- and biostratigraphy across the global Hangenberg Crisis and Devonian–Carboniferous Boundary. *Geol. Soc. Spec. Publ.* **423**, 355–386 (2016).
 15. Caplan, M. L. & Bustin, R. M. Devonian–Carboniferous Hangenberg mass extinction event, widespread organic-rich mudrock and anoxia: causes and consequences. *Palaeogeogr. Palaeoclimatol. Palaeoecol.* **148**, 187–207 (1999).
 16. Marynowski, L., Filipiak, P. & Zatoń, M. Geochemical and palynological study of the Upper Famennian Dasberg event horizon from the Holy Cross Mountains (central Poland). *Geol. Mag.* **147**, 527–550 (2010).
 17. Racka, M. et al. Anoxic Annulata Events in the Late Famennian of the Holy Cross Mountains (Southern Poland): geochemical and palaeontological record. *Palaeogeogr. Palaeoclimatol. Palaeoecol.* **297**, 549–575 (2010).
 18. Tribouillard, N., Algeo, T. J., Lyons, T. & Riboulleau, A. Trace metals as paleoredox and paleoproductivity proxies: an update. *Chem. Geol.* **232**, 12–32 (2006).
 19. Lyons, T. W., Anbar, A. D., Severmann, S., Scott, C. & Gill, B. C. Tracking euxinia in the ancient ocean: a multiproxy perspective and Proterozoic case study. *Annu. Rev. Earth Planet. Sci.* **37**, 507–534 (2009).
 20. Algeo, T. J. & Liu, J. A re-assessment of elemental proxies for paleoredox analysis. *Chem. Geol.* **540**, 119549 (2020).
 21. Bennett, W. W. & Canfield, D. E. Redox-sensitive trace metals as paleoredox proxies: a review and analysis of data from modern sediments. *Earth Sci. Rev.* **204**, 103175 (2020).
 22. Rudnick, R. L. & Gao, S. Composition of the continental crust. *Treatise Geochim.* **3**, 1–64 (2003).
 23. Scott, C., Slack, J. F. & Kelley, K. D. The hyper-enrichment of V and Zn in black shales of the Late Devonian–Early Mississippian Bakken Formation (USA). *Chem. Geol.* **452**, 24–33 (2017).
 24. Aderoju, T. E. & Bend, S. L. Reconstructing the palaeoecosystem and palaeodepositional environment within the Upper Devonian–Lower Mississippian Bakken Formation: a biomarker approach. *Org. Geochem.* **119**, 91–100 (2018).
 25. Stüeken, E. E., Kipp, M. A., Koehler, M. C. & Buick, R. The evolution of Earth's biogeochemical nitrogen cycle. *Earth Sci. Rev.* **160**, 220–239 (2016).
 26. Jenkyns, H. C., Gröcke, D. R. & Hesselbo, S. P. Nitrogen isotope evidence for water mass denitrification during the early Toarcian (Jurassic) oceanic anoxic event. *Paleoceanography* **16**, 593–603 (2001).
 27. Cao, H., Kaufman, A. J. & Shan, X. Coupled isotopic evidence for elevated pCO₂ and nitrogen limitation across the Santonian–Campanian transition. *Chem. Geol.* **504**, 136–150 (2019).
 28. Martinez, A. M., Boyer, D. L., Droser, M. L., Barrie, C. & Love, G. D. A stable and productive marine microbial community was sustained through the end-Devonian Hangenberg Crisis within the Cleveland Shale of the Appalachian Basin, United States. *Geobiology* **17**, 27–42 (2019).
 29. Boyer, D. L. et al. Living on the edge: the impact of protracted oxygen stress on life in the Late Devonian. *Palaeogeogr. Palaeoclimatol. Palaeoecol.* **566**, 110226 (2021).
 30. Abdi, Z., Rimmer, S. M., Rowe, H. D. & Nordeng, S. Controls on organic matter accumulation in the Bakken Formation, Williston Basin, USA. *Chem. Geol.* **586**, 120588 (2021).
 31. Stolper, D. A. & Buchholz, C. E. Neoproterozoic to early Phanerozoic rise in island arc redox state due to deep ocean oxygenation and increased marine sulfate levels. *Proc. Natl Acad. Sci. USA* **116**, 8746–8755 (2019).
 32. Pisarzowska, A. et al. Large environmental disturbances caused by magmatic activity during the Late Devonian Hangenberg Crisis. *Glob. Planet. Change* **190**, 103155 (2020).
 33. Marynowski, L. et al. Deciphering the upper Famennian Hangenberg Black Shale depositional environments based on multi-proxy record. *Palaeogeogr. Palaeoclimatol. Palaeoecol.* **346–347**, 66–86 (2012).
 34. Yao, L. et al. The longest delay: re-emergence of coral reef ecosystems after the Late Devonian extinctions. *Earth Sci. Rev.* **203**, 103060 (2020).
 35. Ward, P., Labandeira, C., Laurin, M. & Berner, R. A. Confirmation of Romer's Gap as a low oxygen interval constraining the timing of initial arthropod and vertebrate terrestrialization. *Proc. Natl Acad. Sci. USA* **103**, 16818–16822 (2006).
 36. Matyja, H., Sobien, K., Marynowski, L., Stempień-Salek, M. & Mąkowski, K. The expression of the Hangenberg Event (latest Devonian) in a relatively shallow-marine succession (Pomeranian Basin, Poland): the results of a multi-proxy investigation. *Geol. Mag.* **152**, 400–428 (2015).
 37. Brom, K. R., Salamon, M. A. & Gorzelak, P. Body-size increase in crinoids following the end-Devonian mass extinction. *Sci. Rep.* **8**, 9606 (2018).
 38. Friedman, M. & Sallan, L. C. Five hundred million years of extinction and recovery: a Phanerozoic survey of large-scale diversity patterns in fishes. *Palaeontology* **55**, 707–742 (2012).
 39. Brocklehurst, N., Kammerer, C. & Frobisch, J. The early evolution of synapsids, and the influence of sampling on their fossil record. *Paleobiology* **39**, 470–490 (2013).
 40. Zhang, F. et al. Multiple episodes of extensive marine anoxia linked to global warming and continental weathering following the latest Permian mass extinction. *Sci. Adv.* **4**, e1602921 (2018).
 41. Stockey, R. G. et al. Persistent global marine euxinia in the early Silurian. *Nat. Commun.* **11**, 1804 (2020).
 42. Pawlik, Ł. et al. Impact of trees and forests on the Devonian landscape and weathering processes with implications to the global Earth's system properties—a critical review. *Earth Sci. Rev.* **205**, 103200 (2020).
 43. Rakociński, M. et al. Mercury spikes as evidence of extended arc-volcanism around the Devonian–Carboniferous boundary in the South Tian Shan (southern Uzbekistan). *Sci. Rep.* **11**, 5708 (2021).
 44. Hetzel, A., Böttcher, M. E., Wortmann, U. G. & Brumsack, H. J. Paleo-redox conditions during OAE 2 reflected in Demerara Rise sediment geochemistry (ODP Leg 207). *Palaeogeogr. Palaeoclimatol. Palaeoecol.* **273**, 302–328 (2009).
 45. Over, D. J. The Devonian–Carboniferous boundary in the United States. *Palaeobiodivers. Palaeoenviron.* **101**, 529–540 (2021).
 46. Sandberg, C. A., Ziegler, W., Leuteritz, K. & Brill, S. M. Phylogeny, speciation and zonation of Siphonodella (Conodonts, Upper Devonian and Lower Carboniferous). *Newsl. Stratigr.* **7**, 102–120 (1978).
 47. Ziegler, W. & Sandberg, C. A. The Late Devonian standard conodont zonation. *Courier Forschungsinstitut Senckenberg* **121**, 1–115 (1990).
 48. Kaiser, S. I., Becker, R. T., Spalletta, C. & Steuber, T. High resolution conodont stratigraphy, biofacies, and extinctions around the Hangenberg Event in pelagic successions from Austria, Italy, and France. *Palaeontographica Americana* **63**, 97–139 (2009).
 49. di Pasquo, M. et al. Palynologic delineation of the Devonian–Carboniferous boundary, West-Central Montana, USA. *Palynology* **41**, 189–220 (2017).
 50. Aretz, M., Corradini, C. & Denayer, J. The Devonian–Carboniferous boundary around the globe: a complement. *Palaeobiodivers. Palaeoenviron.* **101**, 633–662 (2021).

Publisher's note Springer Nature remains neutral with regard to jurisdictional claims in published maps and institutional affiliations.

Springer Nature or its licensor (e.g. a society or other partner) holds exclusive rights to this article under a publishing agreement with the author(s) or other rightsholder(s); author self-archiving of the accepted manuscript version of this article is solely governed by the terms of such publishing agreement and applicable law.

© The Author(s), under exclusive licence to Springer Nature Limited 2023, corrected publication 2023

Article

Methods

Sample collection and preparation

The Sjol, Charlie Sorenson and Abe cores discussed in this paper were drilled in North Dakota at 48.197° N, 103.568° W, 48.139° N, 103.976° W, and 48.240° N, 102.664° W, respectively, by Equinor. The Sjol and Abe cores were described and sampled at Stratum Reservoir Core Facilities in Houston, Texas. The Charlie Sorenson core was sampled at the Bureau of Economic Geology core laboratory in Austin, Texas. Sampling consisted of hand-picking fresh half-core pieces directly from core boxes. The cut and exposed surfaces were ground with Struers Labopol silicon carbide pads to remove surface contamination before being fragmented to small pea-sized chips. For each sample, about 15 g of these chips was crushed to a fine powder using an agate ball mill; residual granules were further powdered with an agate mortar and pestle. At no time did the samples come into contact with metal surfaces that might contaminate the powders during sample preparation.

Iron speciation

Iron speciation analyses were conducted at George Mason University and the University of Maryland following published methods⁵¹. Pyrite iron (Fe_{py}) was calculated (assuming a stoichiometry of FeS_2) from the mass of silver sulfide precipitated during a 3-h hot chromous chloride distillation⁵². For these extractions, a chromium reduction solution (CRS) was prepared with 260 g $\text{Cr}(\text{III})\text{Cl}_3 \cdot 6\text{H}_2\text{O}$, 150 g Zn granules and 500 ml of 0.5 N hydrochloric acid (HCl). Reactions were conducted under a stream of ultra-high-purity (UHP) N_2 with 20 ml of 5 N HCl and 20 ml CRS, with evolved hydrogen sulfide passed through Milli-Q (18 MΩ) water, to absorb acids, and a 0.3 M silver nitrate trapping solution. Other iron species—specifically, iron carbonate (Fe_{carb}), iron oxy(hydroxides) (Fe_{ox}) and magnetite (Fe_{mag})—were extracted sequentially⁵¹. Approximately 100 mg of sample powder was first reacted with a 1 M sodium acetate solution buffered with acetic acid to a pH of 4.5. The extraction lasted for 48 h. After decanting the solution, the sample powder was then subjected to a 50 g l⁻¹ sodium dithionite solution buffered with 0.35 M acetic acid and 0.2 M sodium citrate to a pH of 4.8. The extraction lasted for 2 h. Lastly, after decanting the previous solution, the sample powder was subjected to a 0.2 M ammonium oxalate, 0.17 M oxalic acid solution buffered to a pH of 3.2. The extraction lasted for 6 h. These three solutions are designed to extract Fe_{carb} , Fe_{ox} and Fe_{mag} , respectively. The ammonium oxalate solution has also been shown to extract iron-rich clay minerals⁵³. The sequential extracts were analysed with an Element 2 inductively coupled plasma mass spectrometer (ICP-MS) at the University of Maryland using scandium as an internal standard to monitor signal suppression. 2 standard deviations of duplicates that were separately subjected to the entire process of sequential extraction and ICP-MS analysis was better than 0.063 wt% for Fe_{carb} , 0.003 wt% for Fe_{ox} and 0.006 wt% for Fe_{mag} . As discussed in the following section, total iron concentrations (Fe_t) were determined by multi-acid digestion followed by ICP-MS analysis from the commercial laboratory Bureau Veritas.

Elemental analysis

In this study, a full suite of major, trace and rare-earth element data were generated from bulk powders sent to the commercial laboratory Bureau Veritas. The samples were ashed, digested using a multi-acid procedure, and analysed via ICP-MS using the Bureau Veritas preparation code MA-250 IGN. The relative standard deviation of replicate measurements of the standard reference material OREAS 45e for the main elements of interest was 2.67% for Mo, 4.68% for Zn, 3.92% for Fe, 3.96% for U and 2.47% for V. There is <0.002 ppm Re in the OREAS 45e standard, but we used the average of sample replicates to calculate a relative standard deviation of 3.69% for Re. Mercury was analysed by Bureau Veritas using the preparation code CV402 (cold vapour method). Replicate measurements of the standard reference materials

OREAS 620 and OREAS 623 produced relative standard deviations of 4.19% and 6.69%, respectively.

X-ray fluorescence

Premier OilField Group (POFG) provided most of the XRF dataset (see below for additional compilation sources). Elemental analysis on core and drill cuttings was performed using a Bruker S2 Ranger Tabletop ED-XRF instrument. Further details are available at the POFG website (<https://pofg.com/wp-content/uploads/2019/02/XRF-Tech-Note-17.pdf>). The major elements reported (11) are Na, Mg, Al, Si, P, S, K, Ca, Ti, Mn and Fe. The trace elements reported (18) are V, Cr, Co, Ni, Cu, Zn, Ga, As, Se, Rb, Sr, Zr, Nb, Mo, Ba, Pb, Th and U. Typical resolution is 145 eV at 100,000 cps.

We compared our data for Mo and V concentrations from the ICP-MS and XRF methods to assess the validity of presenting ICP-MS data for the Sjol and Charlie Sorenson cores and using XRF data for our basin-wide compilations. As seen in Supplementary Fig. 8, there is excellent agreement between the two methods for both Mo and V concentrations when plotted against stratigraphic depth. A cross-plot is also presented for both Mo and V data obtained using the ICP-MS and XRF methods (Supplementary Fig. 8). The correlation between the two methods is $R^2 = 0.74$ and $R^2 = 0.91$ for Mo and V, respectively. Element concentrations were measured using the two methods on different samples, however, so making this cross-plot requires a depth adjustment, thus explaining the lower R^2 values than would be expected if the two measurements were performed on the exact same samples. Overall, the strong agreement between the two methods justifies our use of both methods for the interpretations made in this study.

TOC, TN, organic carbon and nitrogen isotopes

For these analyses, carbonate was quantitatively removed from bulk powders (about 2–3 g) by repeated treatment with 3 M HCl and washed with 18-MΩ Milli-Q water (3–4 times) to neutralize the solution and produce insoluble residues primarily containing silicates, pyrite and total organic matter. The solutions were decanted and the residues dried overnight at 80 °C. The residues were then weighed to determine the percentage of carbonate. The abundance and C/N isotopic composition of the residues were subsequently determined by combustion to CO_2 and N_2 with a Eurovector elemental analyser in-line with an Elementar continuous flow Isoprime isotope ratio mass spectrometer (IRMS) in the Paleoclimate Co-Laboratory at the University of Maryland. Between 0.5 mg and 2 mg of the homogenized residues were weighed, transferred and folded into 3 × 5 mm tin cups. Samples were sequentially dropped into a 1,040 °C quartz combustion column along with a timed pulse of oxygen and a constant flow of helium carrier gas (about 100 ml min⁻¹). Combustion products travelled through the reaction tube packed with silvered cobalt (II/III) oxide, chromium oxide and quartz chips for quantitative oxidation to carbon dioxide (CO_2) and nitrous oxides, which were reduced to N_2 in a second quartz column at 650 °C filled with reduced copper wire and quartz chips. Water produced during the reactions was removed via a 10-cm magnesium perchlorate column, and the N_2 gas was separated from CO_2 in a 0.7-m stainless steel gas chromatograph column packed with molecular sieve heated to 60 °C. The retention time for analytes was about 95 s (for N_2) and about 230 s (for CO_2). The sample N_2 peak was preceded by a 30-s reference N_2 gas injection beginning at 20 s into each cycle, while the sample CO_2 peak was followed by a 30-s reference CO_2 gas injection, for a total analysis time of 450 s. The N_2 and CO_2 isotopic ratios are determined by integrating peak areas of m/z 28, 29 and 30 (for N_2) and 44, 45 and 46 (for CO_2) for reference and sample pulses, relative to baseline. Isotopic ratios are expressed in the delta notation as per mil deviations from the V-AIR (Vienna AIR) and VPDB (Vienna Pee Dee Belemnite) standards. Measurement uncertainties, typically better than ±0.2% (1 s.d.) for both isotopes, are determined by interspersed analyses ($n \geq 8$) of the LECO 062 and 309 soil standards during each

analytical session. The TOC and TN of bulk samples were then calculated by multiplying the percent C and percent N of the residue aliquots by the percent residue determined gravimetrically by acidification.

Pyrite sulfur isotopes

The sulfur abundance and isotopic composition of pyrite were measured by first weighing, placing and folding between 0.3 mg and 0.5 mg of silver sulfide (produced during the CRS extraction described above) into 3×5 mm tin cups (with addition of about 0.2 mg V_2O_5 as an oxidant). These were sequentially dropped in the same elemental analyser–IRMS system with a timed pulse of O_2 and a constant flow of helium carrier gas (about 100 ml min^{-1}) into a quartz column packed with high-purity reduced copper wire heated to $1,040^\circ\text{C}$. The sulfur dioxide (SO_2) analyte was swept through a $Mg(ClO_4)_2$ desiccant column to remove water and separated from other gases with a 1-m Teflon gas chromatograph column packed with Porapak-Q heated to 115°C . A timed pulse of SO_2 reference gas (Airgas 99.999% purity, about 6 nA) was introduced at the beginning of the run using an injector connected to the IRMS with a fixed open ratio split. The isotope ratios of reference and sample peaks were determined by monitoring ion-beam intensities relative to background values. Isotopic results are expressed in delta notation as per mil (‰) deviations from the Vienna Canyon Diablo Troilite (VCDT) standard. Two NBS-127 standards and two NZ-1 standards were measured between each set of 10 samples, and uncertainties for each analytical session based on these standard analyses were better than 1.0% and 0.3%, respectively, for abundance and isotopic compositions. Total sulfur contents of bulk samples were calculated by quantifying IRMS SO_2 peak areas relative to those from measured amounts of standard materials and the percent residue.

XRF compilation

XRF data compilations are composed of three datasets: (1) POFG-analysed 75 drill cores, (2) literature data compilations of 13 drill cores, and (3) Sjol and Abe core independent XRF analysis. The locations of the POFG wells (Supplementary Table 1a) along with literature compilations used in our XRF data compilation study (Supplementary Table 1b) are presented in Extended Data Fig. 3. In addition, locations of wells used for Fig. 4 are summarized in Supplementary Table 1c. For POFG details, see <https://www.pofg.com>.

Subunit classification

In the absence of biostratigraphy and ultrahigh-resolution conodont zonation, the classification of LB1, LB2 and LB3 in all wells was delineated by a sequence of decision trees. Most of the sections have a clear carbonate concretion layer that denotes a marker bed between LB2 and LB3 (see core photos in Supplementary Fig. 5; ref.¹¹). However, we do not have access to all 90 drill cores, and hence we used wt% calcium (Ca) as a proxy for carbonate presence. In most cases, we interpret wt% Ca > 4.5 as indicative of carbonate. To add confidence to the interpretation, we added wireline logs for better refined boundaries. Carbonate layers, although thin, do appear as intervals of higher density (Supplementary Fig. 1), which provide well-defined boundaries between subunits. In cases where carbonate is absent or the wireline density logs are low resolution, low [Al] (detrital proxy) and Al/Si ratio is used to define subunit boundaries. The presence of a carbonate concretion layer is relatively less abundant at the LB1/LB2 boundary across the basin. It is important to note that the thickness map of the LBS also aids our interpretation, along with the core photos and wt% Ca. The centre of the basin is the thickest and also contains LB1, followed by LB2, and, ultimately, LB3. A few notable sections, such as Charlie Sorenson, Leo and Person¹¹, are already in the published literature and we used our decision tree (on the basis of geochemical and petrophysical data) to make delineations of LB1, LB2 and LB3 in each of the other cores. For the classification of the UBS (UB1 and UB2), our approach was based on sedimentological and geochemical characteristics as presented in

refs.^{54,55}. We integrated our LBS workflow for detailed classifications of UB1 and UB2 (and even subunits UB1A, UB1B, UB2A and UB2B).

Mass-balance modelling

A simplistic mass-balance model was applied to better understand the effects of extreme euxinic conditions on the Mo cycle during the Hangenberg Event. We build on concepts and models presented by refs.^{56,57}, where a first-order model is created based on modern Mo seawater sources and sinks (equation (1)). Whereas input fluxes for Mo are primarily riverine input, the output fluxes are strongly dependent on reducing environments (oxic, suboxic and euxinic), and we therefore assume that burial rates (b) in each individual Mo sink (i) scale with [Mo] inventory (equation (4)). Mo removal fluxes (F) in each sink are also scaled to their respective seafloor coverage (A)—a first-order or direct feedback model^{56,57} (equation (5)). Keeping to a simplistic model approach that allows us to make broad-scale interpretations of our dataset, we have not considered any variability in the burial factor as proposed by ref.⁵⁸. Time-series solutions are represented by equation (7). Equations, variables and constants used in our model are described here:

$$\int_0^v [Mo] dV = J_{in} - J_{out} \quad (1)$$

$$\int_0^v [Mo] dV = F_{in} - F_{out} \quad (2)$$

$$v \times \frac{dC_{Mo}}{dt} = J_r - [F_{so} + F_o + F_{ex}] \quad (3)$$

$$b_i = b_{i0} \times \left[\frac{Mo}{Mo_0} \right] \quad (4)$$

$$F_i = A_i \times b_i \quad (5)$$

$$\frac{dC_{Mo}}{dt} = \lambda - \gamma \times [Mo] \quad (6)$$

$$[Mo]_t = [Mo]_x + (Mo_0 - Mo_x) \times e^{-\gamma t} \quad (7)$$

The seafloor area is between 3.50×10^8 and $3.61 \times 10^8 \text{ km}^2$ and the ocean volume is between 1.30×10^{18} and $1.37 \times 10^{18} \text{ m}^3$. V and v both represent global ocean volume. J_{in} and J_{out} represent the mass of Mo entering and exiting the system, respectively. J_r is the river source, F_{in} and F_{out} are the source and sink fluxes, respectively, F_{so} is the suboxic flux, F_o is the oxic flux, F_{ex} is the euxinic flux, $\lambda = F_{source}$ and $\gamma = F_{sinks}$, t represents any given time, and $x = \text{terminal} = \lambda/\gamma(F_{source}/F_{sinks})$.

Model simulations were run in MATLAB (MathWorks, 2019) and codes written for this paper are available at <https://github.com/swapankr-sahoo/hangenberg> and <https://doi.org/10.5281/zenodo.7293587>. We have provided a simple model and the user can change parameters to test multiple scenarios.

Modelling results

Our model (Extended Data Fig. 4) shows the effects of changes in the amount of global seafloor euxinic area on the aqueous Mo concentration ($[Mo]_{aq}$) of the global ocean. If we assume a starting $[Mo]_{aq}$ of 105 nmol l^{-1} , which is the same as the modern ocean value, we see that expanding euxinic area to 0.5% of the global seafloor (as opposed to 0.05% today) will draw down $[Mo]_{aq}$ of the oceans to about 80 nmol l^{-1} in 200 kyr and to about 65 nmol l^{-1} in 500 kyr. The latter time frame results in the ocean $[Mo]_{aq}$ being reduced to 62% of its initial value. The effects on seawater $[Mo]_{aq}$ are even more marked as seafloor euxinic area increases. At a seafloor euxinic area of 1%, $[Mo]_{aq}$ of the oceans will

Article

be reduced to about 65 nmol l⁻¹ and about 40 nmol l⁻¹ over 200 kyr and 500 kyr, respectively. This would leave only 62% and 38% of the initial Mo inventory of the oceans after 200 kyr and 500 kyr, respectively. At a seafloor euxinic area of 2%, [Mo]_{aq} of the oceans will be reduced to about 35 nmol l⁻¹ and about 20 nmol l⁻¹ over 200 kyr and 500 kyr, respectively. This would leave only 33% and 19% of the initial Mo inventory of the oceans after 200 kyr and 500 kyr, respectively. Clearly, only a small-scale expansion of global euxinia is needed to completely draw down the Mo inventory of the global oceans.

Using the Mo/TOC ratio of our samples from the Bakken Shale, we can estimate [Mo]_{aq} in the Williston Basin at various points in the basin's history. For this exercise, we focused on LB3 because it represents the maximum expansion of euxinia during the Hangenberg Black Shale Event. A previous study⁵⁹ found that sediment Mo/TOC scales with deep-water [Mo]_{aq} in modern restricted euxinic basins. Data from the Saanich Inlet, Cariaco Basin, Framvaren Fjord and Black Sea produced an R^2 value of 0.96 for the regression line between average sediment Mo/TOC (plotted on a log scale) and average deep-water [Mo]_{aq}. We used this relationship applied to Mo/TOC ratios in LB3 to estimate deep-water [Mo]_{aq} in the Williston Basin at the time of the Hangenberg Event. The median Mo/TOC ratio of all LB3 samples from all wells in the XRF compilation is 30.6, with a 25th percentile value of 25.2 and a 75th percentile value of 39.5 (Extended Data Fig. 4). This corresponds to a deep-water [Mo]_{aq} value in the Williston Basin of about 65 nmol l⁻¹, about 75 nmol l⁻¹ and about 85 nmol l⁻¹, respectively, for the 25th percentile, median and 75th percentile Mo/TOC values of LB3 based on the regression line of ref.⁵⁹. We then assessed which of our modelling scenarios fit with these estimated aqueous Mo concentrations. At 2% seafloor euxinic area, [Mo]_{aq} would be drawn down to about 40 nmol l⁻¹ over ~200 kyr, which is estimated to be the maximum duration of the Hangenberg Event⁶⁰. This is inconsistent with Mo/TOC ratios in LB3, which indicate a [Mo]_{aq} value of about 65 nmol l⁻¹ even at the 25th percentile of Mo/TOC. This suggests that even if there was unlimited exchange of Mo between open seawater and the Williston Basin during deposition of LB3, the global seafloor euxinic area must have been less than 2%. We take our estimate of [Mo]_{aq} in the Williston Basin as a minimum for global seawater because limited exchange would lead to lower [Mo]_{aq} in the Williston Basin compared with the open ocean. If the open ocean had higher [Mo]_{aq} than the Williston Basin waters, it only emphasizes our point that 2% seafloor euxinic area is too high to be consistent with our model.

Instead, our model results fit best with seafloor euxinic area values between 0.5% and 1% during the Hangenberg Event. These results emphasize that although euxinic expansion in shallow, nearshore areas was probably an important kill mechanism in the Late Devonian extinctions, it does not imply that euxinia was a whole-ocean phenomenon. A previous study⁶¹ estimated that >5% of the global seafloor became anoxic during the Hangenberg Event based on U isotopes in marine carbonates. Recent data suggest that U isotopes may be specifically sensitive to euxinia as opposed to general anoxia^{62,63}, however, such that the U isotope modelling of ref.⁶¹ may imply a seafloor euxinic area of >5% during the Hangenberg Event. By contrast, our Mo concentration and Mo/TOC data from LB3 suggest that 5% seafloor euxinic area is a significant overestimate. Under this scenario, the strong Mo enrichments seen in LB3 would not be possible because the Mo inventory of the global oceans would be substantially drawn down. Alternatively, it is possible that the >5% estimate of general anoxic seafloor⁶¹ is correct and only a small fraction of that anoxic seafloor was euxinic. That would make our model results compatible with the model results of ref.⁶¹. Future work should focus on reconciling models based on multiple independent proxies derived from different lithologies for the same intervals in Earth history. Ultimately, we suggest that the D/C transition represents a unique interval in Earth history when there was a locus of euxinia in shallow epicontinental seas, and that the nearshore location of these euxinic loci was more important than the total euxinic area

of the global oceans. This locus of euxinic expansion in the shallow habitable zone of the oceans probably contributed to the pattern and severity of Late Devonian mass extinction.

Upper Bakken Shale results and interpretations

In the Lower Carboniferous UBS, subunit UB1 comprises a transgressive systems tract and UB2 represents a highstand systems tract deposited during maximum flooding near the base of the *Si. quadruplicata* Zone (Fig. 1). Regression during the D/C boundary glaciation⁶ is represented by MB1, and broadly, the UBS represents continued transgression after initial sea-level rise in MB2. Iron speciation indicates persistently euxinic environments throughout deposition of the UBS with the up-section decline in Fe_{HR}/Fe_T (where Fe_{HR} indicates highly reactive iron), probably reflecting increased sedimentation rates as environments prograded seawards⁴³. Unlike the LBS, Mo concentrations are progressively drawn down through the UBS and behave antithetically to those of V (Fig. 2), which rise through the interval and culminate in strong enrichments (>2,000 ppm) in UB2. The metal inventory of a basin is controlled by the complex interplay between anoxic/euxinic drawdown and deep-water renewal⁵⁹, and the result need not be the same for Mo and V given the same boundary conditions. The generally higher V enrichments in the UBS compared with the LBS could also reflect a higher oceanic V inventory, which resulted from enhanced Mn cycling and release of V to the water column (see refs.^{56,59}) during D/C boundary glaciation. TOC and TN concentrations are constant around 10 wt% and 0.4 wt%, respectively, in both UB1 and UB2, which are lower than maximal values in the LBS and may also be related to dilution. $\delta^{15}\text{N}$ values hover around 0‰ in UB1, but increase to nearly +2‰ at the base of UB2, indicating a local intensification of anoxia or influx of isotopically heavy N from the open ocean, most likely associated with maximum transgression. $\delta^{34}\text{S}_{\text{py}}$ values also progressively decrease through the UBS, except for the lowermost few samples that are potentially related to a continental weathering flux associated with the D/C boundary lowstands. Analogous to the LBS, the $\delta^{34}\text{S}_{\text{py}}$ trend can be interpreted as both a flushing of the basin with marine sulfate and an expansion of water-column euxinia. Despite minor differences, the broad geochemical patterns recorded in both the LBS and UBS indicate that stepwise marine transgression is associated with progressive intensification of water-column euxinia. In the case of the Tournaisian episode, euxinia may have hindered ecosystem recovery after the Hangenberg Event, evidenced by the lack of metazoan reef constructions⁶⁴.

Similar to the maps presented in Fig. 3 and discussed in the main text, we also produced gridded heat maps for Mo and V concentrations for the UBS. As indicated by our heat maps (Extended Data Fig. 5), Mo reached its highest levels in shallow-water environments during deposition of UB1, followed by a decline in Mo concentrations in UB2. This is consistent with a flushing of metals into the Williston Basin from the open ocean upon transgression, which, combined with locally euxinic bottom waters, led to strong Mo enrichment in sediments of UB1. Indeed, the highest UBS Mo concentrations in the Sjol core occur at the base of UB1 (Fig. 2). Molybdenum concentrations decline up-section through the UBS, however, which we attribute to: (1) drawdown of aqueous Mo concentrations because euxinia was still widespread across the basin, and (2) dilution because of increasing sedimentation rate and silt input⁵⁴. Several other geochemical parameters such as wt% pyrite S and Fe_{HR}/Fe_T also show evidence for dilution up-section in the UBS.

Vanadium concentrations are also high in UB1, but contrary to the behaviour of Mo, V abundances get even higher in UB2, reaching the level of 'hyper-enrichment' seen in LB3 during the Hangenberg Event (Supplementary Fig. 21). This occurs despite potential dilution by increasing siliciclastic input. When looking at a cross-plot of Mo versus U enrichment factors (Supplementary Figs. 12–15), we see that most parts of the Bakken Shale do not fall in the field indicating a Mn–Fe-oxyhydroxide shuttle. The only subunit that does show a substantial cloud of data points in the particulate shuttle field, however,

is UB2 (Supplementary Fig. 16). Strong V enrichment in UB2 could therefore be related to particulate shuttling. This would be expected to affect Mo delivery as well, but only if sufficient Mo was available in the water column. This hypothesis is admittedly speculative and requires further testing, which could be achieved using isotope systems such as Mo and thallium that are sensitive to oxide shuttling. Another important point is that the oceans were clearly replete with V during deposition of the UBS. As mentioned previously, the generally higher V enrichments in the UBS compared with the LBS could also reflect a higher V inventory in the post-glacial ocean, which resulted from enhanced Mn cycling and release of V to the water column during glaciation^{56,65}.

Data availability

All geochemical data generated here are publicly available at <https://doi.org/10.5281/zenodo.7379380>. Splits of samples are reposed at Equinor US and George Mason University and are available upon request.

Code availability

Code (in MATLAB) for the Mo mass-balance model is available on GitHub at <https://github.com/swapankrshahoo/hangenberg> and on Zenodo at <https://doi.org/10.5281/zenodo.7293587>.

51. Poulton, S. W. & Canfield, D. E. Development of a sequential extraction procedure for iron, implications for iron partitioning in continentally derived particulates. *Chem. Geol.* **214**, 209–221 (2005).
52. Canfield, D. E., Raiswell, R., Westrich, J. T., Reaves, C. M. & Berner, R. A. The use of chromium reduction in the analysis of reduced inorganic sulfur in sediments and shales. *Chem. Geol.* **54**, 149–155 (1986).
53. Slotnick, S. P. et al. Unraveling the mineralogical complexity of sediment iron speciation using sequential extractions. *Geochem. Geophys. Geosyst.* **21**, e2019GC008666 (2020).
54. Nandy, D. *Dolomitization and Porosity Evolution of Middle Bakken Member, Elm Coulee Field and Facies Characterization, Chemostratigraphy and Organic-richness of Upper Bakken Shale, Williston Basin* (Colorado School of Mines, 2018).
55. Borcovsky, D. et al. Sedimentology, facies architecture, and sequence stratigraphy of a Mississippian black mudstone succession—the upper member of the Bakken Formation, North Dakota, United States. *AAPG Bull.* **101**, 1625–1673 (2017).
56. Sahoo, S. K. et al. Ocean oxygenation in the wake of the Marinoan glaciation. *Nature* **489**, 546–549 (2012).
57. Gilleaudeau, G. J. & Kah, L. C. Oceanic molybdenum drawdown by epeiric sea expansion in the Mesoproterozoic. *Chem. Geol.* **356**, 21–37 (2013).
58. Reinhard, C. T. et al. Proterozoic ocean redox and biogeochemical stasis. *Proc. Natl Acad. Sci. USA* **110**, 5357–5362 (2013).
59. Algeo, T. J. & Lyons, T. W. Mo-total organic carbon covariation in modern anoxic marine environments: implications for analysis of paleoredox and paleohydrographic conditions. *Paleoceanography* **21**, PA1016 (2006).
60. Myrow, P. M. et al. High-precision U-Pb age and duration of the latest Devonian (Famennian) Hangenberg Event, and its implications. *Terra Nova* **26**, 222–229 (2014).
61. Zhang, F. et al. Extensive marine anoxia associated with the Late Devonian Hangenberg Crisis. *Earth Planet. Sci. Lett.* **533**, 115976 (2019).
62. Gilleaudeau, G. J. et al. Uranium isotope evidence for limited euxinia in mid-Proterozoic oceans. *Earth Planet. Sci. Lett.* **521**, 150–157 (2019).
63. Cole, D. B. et al. Uranium isotope fractionation in non-sulfidic anoxic settings and the global uranium isotope mass balance. *Glob. Biogeochem. Cycles* **34**, e2020GB006649 (2020).
64. Yao, L., Aretz, M., Chen, J., Webb, G. E. & Wang, X. Global microbial carbonate proliferation after the end-Devonian mass extinction: mainly controlled by demise of skeletal bioconstructors. *Sci. Rep.* **6**, 39694 (2016).
65. Hastings, D. W., Emerson, S. R. & Mix, A. C. Vanadium in foraminiferal calcite as a tracer for changes in the areal extent of reducing sediments. *Paleoceanography* **11**, 665–678 (1996).
66. Kaiser, S. I., Becker, R. T., Steuber, T. & Aboussalam, S. Z. Climate-controlled mass extinctions, facies, and sea-level changes around the Devonian–Carboniferous boundary in the eastern Anti-Atlas (SE Morocco). *Palaeogeogr. Palaeoclimatol. Palaeoecol.* **310**, 340–364 (2011).
67. Girard, C., Cornee, J., Corradini, C., Fravalo, A. & Feist, R. Palaeoenvironmental changes at Col des Tribes (Montagne Noire, France), a reference section for the Famennian of north Gondwana-related areas. *Geol. Mag.* **151**, 864–884 (2014).
68. Zhang, X., Over, D. J., Ma, K. & Gong, Y. Upper Devonian conodont zonation, sea-level changes and bio-events in offshore carbonate facies Lali section, South China. *Palaeogeogr. Palaeoclimatol. Palaeoecol.* **531**, 109219 (2019).
69. Frey, L., Rücklin, M., Korn, D. & Klug, C. Late Devonian and Early Carboniferous alpha diversity, ecospace occupation, vertebrate assemblages and bio-events of southeastern Morocco. *Palaeogeogr. Palaeoclimatol. Palaeoecol.* **496**, 1–17 (2018).

Acknowledgements This work was supported by Equinor US. We thank K. Hlava and V. Hallam at Equinor US for providing samples and access to core data; R. Ash and J. Farquhar at the University of Maryland for ICP-MS support and access to CRS extraction lines, respectively; Z. He for valuable discussion on data analytics and usage of Trinity software (Zetaware) package; R. Womack and K. J. Gomez for ArcGIS and Ocean Data View software support; H. Jin for sharing his thesis dataset; D. Nandy for several discussions on the Bakken stratigraphy; P. Sadler and N. Hogancamp for discussion on biostratigraphy; and D. J. Over for conodont consultation at Equinor US.

Author contributions S.K.S., G.J.G. and A.J.K. conceived the idea and concepts. Samples were collected by S.K.S., G.J.G., A.J.K. and A.B. A.J.K. performed the bulk of laboratory analyses with additional analyses performed by G.J.G. T.F. provided laboratory support. A.J.K. provided conceptual insight into biogeochemical data interpretation. B.H. provided insight into core description and general geology. B.D.B. provided insight into stratigraphic correlations and T.L. provided additional samples and insight into XRF methodology. A.B. performed initial conodont studies. S.K.S. and K.W. performed the statistical data analysis and numerical models. G.J.G., S.K.S. and A.J.K. wrote the manuscript, with important contributions from B.H. and B.D.B. All authors contributed to editing the manuscript and validating the concepts and models.

Competing interests The authors declare no competing interests.

Additional information

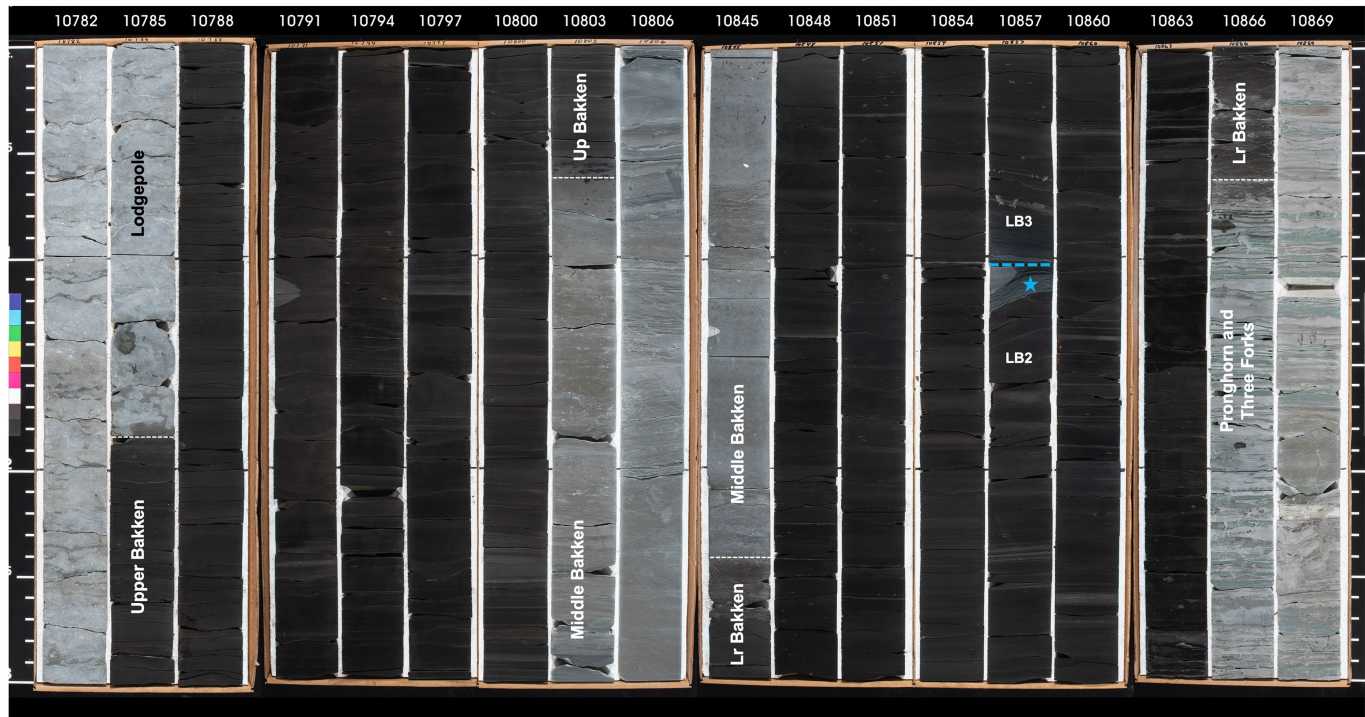
Supplementary information The online version contains supplementary material available at <https://doi.org/10.1038/s41586-023-05716-2>.

Correspondence and requests for materials should be addressed to Swapan K. Sahoo.

Peer review information *Nature* thanks Phoebe Cohen, Sandra Kaiser, Leszek Marynowski and Eva Stueken for their contribution to the peer review of this work.

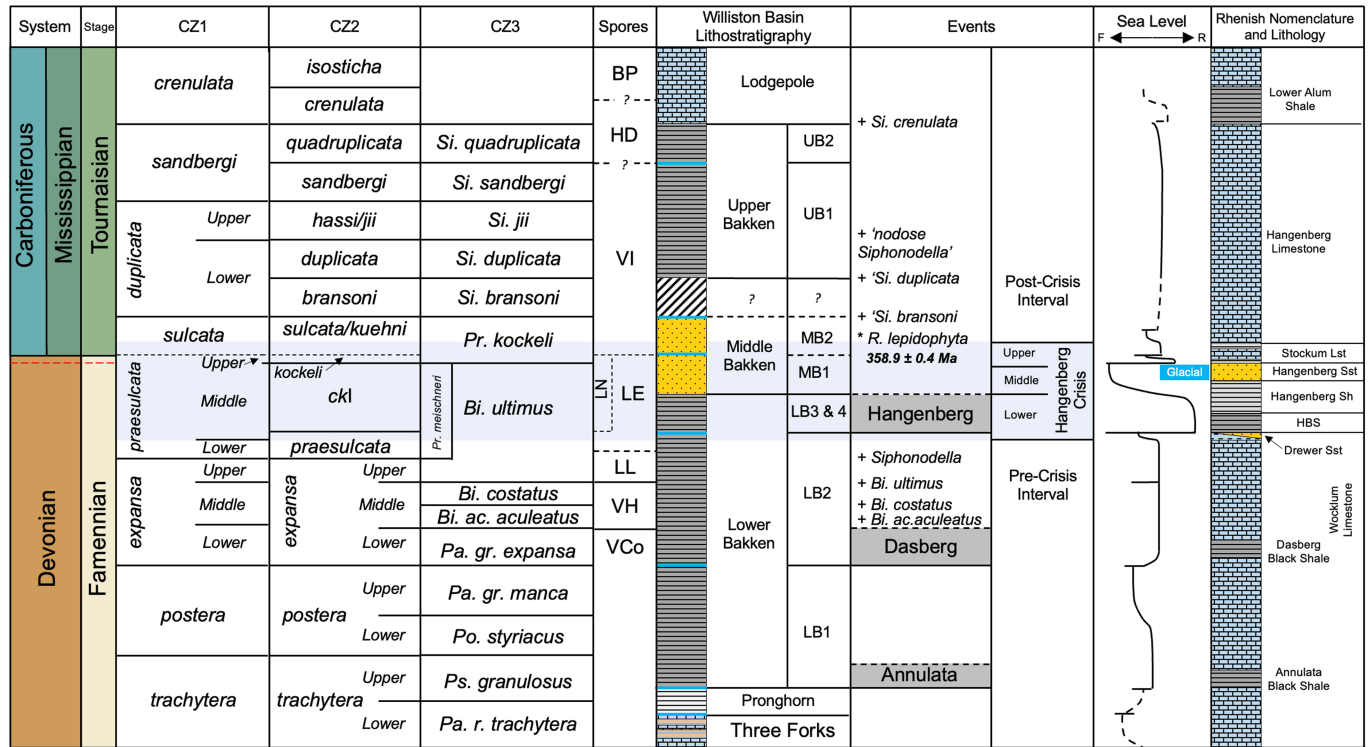
Reprints and permissions information is available at <http://www.nature.com/reprints>.

Article



Extended Data Fig. 1 | Core photographs for the Sjol core. Photos were taken by Stratum Reservoir at the Houston facility. Each box holds approximately 1 m (3 ft.) and the numbers at the top of each row represent the core depth in feet. We have not exhibited the full MB as it is not the focus of this study (the 10809–10845 ft. interval is not presented here). Individual formations are

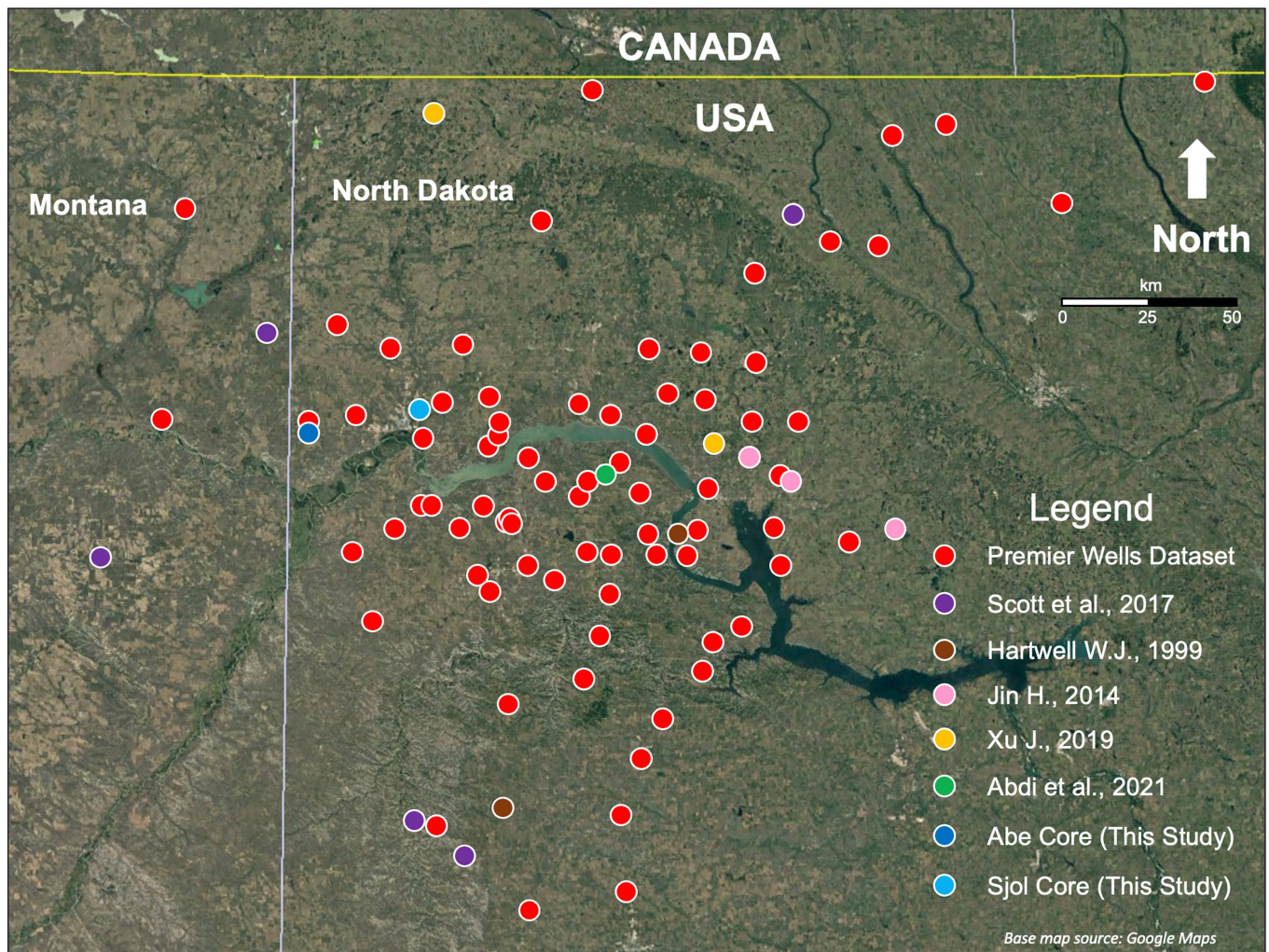
labelled on the photographs, with dashed white lines indicating unit boundaries. The blue star denotes the presence of a carbonate-rich horizon, which is traceable basin-wide as a marker between LB2 and LB3, here shown as the blue dashed line.



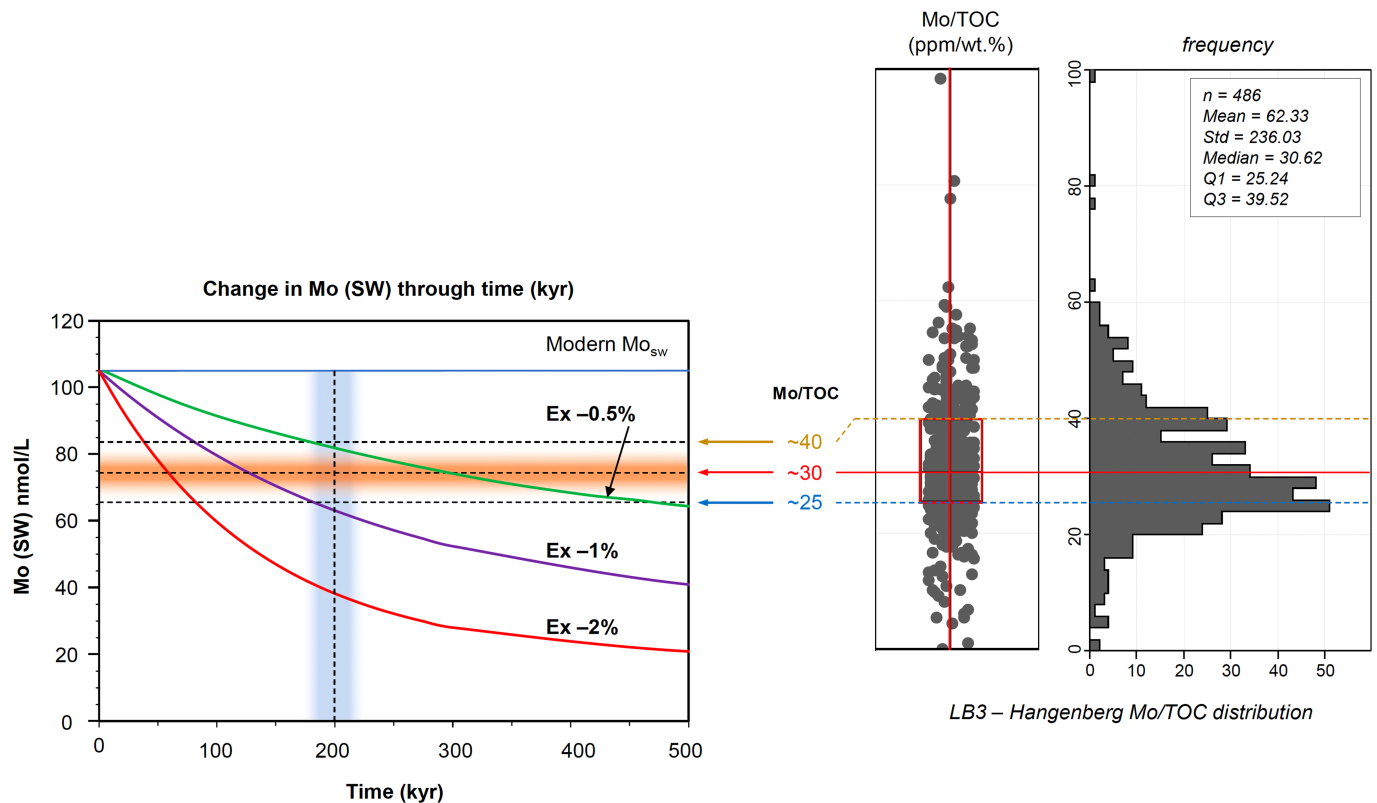
Extended Data Fig. 2 | Integrated stratigraphy of the Devonian–Carboniferous transition.

Bio- and lithostratigraphic constraints, along with sea-level history, climate, and comparison between the Williston Basin and the

classic Rhenish Massif section of Germany. Conodont zonation schemes and abbreviations are described in Fig. 1. Sea-level history compiled based on ref. 8,66–69. Rhenish nomenclature and lithology based on refs. 7,14,66.

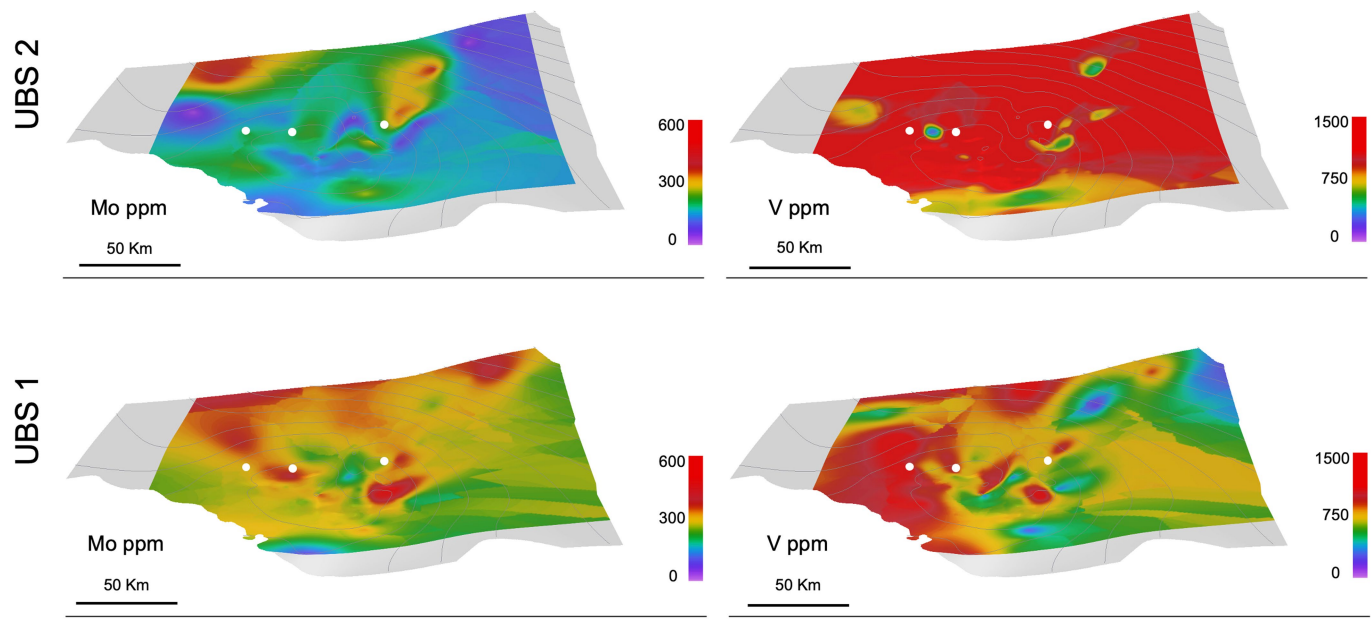


Extended Data Fig. 3 | Location of all wells used in XRF compilation study. Well locations from various sources in northwestern North Dakota and northeastern Montana are represented by coloured dots with the USA-Canada border shown at the top. The map is taken from Google Maps.



Extended Data Fig. 4 | Mass-balance model results for seawater $[Mo]_{aq}$ changes over time in response to expansion of seafloor euxinic area (Ex). $[Mo]_{aq}$ in the Williston Basin during the Hangenberg Event is estimated from Mo/TOC ratios in LB3 sediments. This is based on empirical data from modern euxinic basins where the relationship between deep-water $[Mo]_{aq}$ and sediment Mo/TOC is expressed with the equation $Mo/TOC = 4.7389e^{25.457x}$,

where $x = [Mo]_{aq}$ (ref. ⁵⁹). To test differences in model results across the spread of Mo/TOC ratios recorded in LB3, we explored the 25th percentile, median and 75th percentile Mo/TOC values (seen in box and whisker plot on the right and covered by the orange horizontal shading on the left). Maximum duration of the Hangenberg Event was estimated at ~200 kyr by ref. ⁶⁰. This time frame is highlighted by the blue vertical shading.



Extended Data Fig. 5 | Gridded heat maps for Mo and V concentrations across UB1 and UB2. Mo is on the left and V is on the right. UB1 is on the bottom and UB2 is on the top. These graphics are analogous to the gridded heat maps for the LBS presented in Fig. 3. Trinity (T3) software was used to produce these maps and 3D visualization. Note that there are map artifacts of carbonate

concretion-rich zones where metals are of low concentration. Although any wt.% Ca > 4.5% was removed from our calculations, some artifacts remain and should be interpreted carefully. Three white dots in each map represent three well locations (from west to east: Abe, Sjol and Charlie Sorenson).